

Transformation of Active Sites in Fe/SSZ-13 SCR Catalysts during Hydrothermal Aging: A Spectroscopic, Microscopic, and Kinetics Study

Libor Kovarik,[†] Nancy M. Washton,[†] Ravi Kukkadapu,[†] Arun Devaraj,[†] Aiyong Wang,[‡] Yilin Wang,[‡] Janos Szanyi,[‡] Charles H. F. Peden,[‡] and Feng Gao^{*,†}

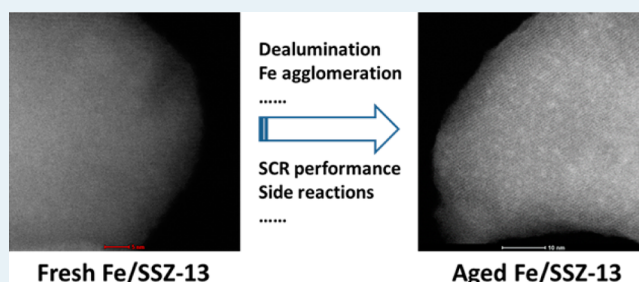
[†]Environmental Molecular Sciences Laboratory, Pacific Northwest National Laboratory, P.O. Box 999, Richland, Washington 99354, United States

[‡]Institute for Integrated Catalysis, Pacific Northwest National Laboratory, P.O. Box 999, Richland, Washington 99354, United States

S Supporting Information

ABSTRACT: Fe/SSZ-13 catalysts (Si/Al = 12, Fe loadings of 0.37% and 1.20%) were prepared via solution ion-exchange, and they were hydrothermally aged at 600, 700, and 800 °C. The fresh and aged catalysts were characterized with surface area/pore volume analysis, Mössbauer, solid-state MAS NMR, NO titration FTIR spectroscopies, and TEM and APT imaging. Hydrothermal aging causes dealumination of the catalysts and transformation of various Fe sites. The latter include conversion of free Fe²⁺ ions to dimeric Fe(III) species, the agglomeration of isolated Fe-ions to Fe-oxide clusters, and incorporation of Al into the Fe-oxide species. These changes result in complex influences on standard SCR and NO/NH₃ oxidation reactions. In brief, mild aging causes catalyst performance enhancement for SCR, whereas harsh aging at 800 °C deteriorates SCR performance. In comparison to Fe/zeolites more prone to hydrothermal degradation, this study demonstrates that via the utilization of highly hydrothermally stable Fe/SSZ-13 catalysts, more accurate correlations between various Fe species and their roles in SCR related chemistries can be made.

KEYWORDS: selective catalytic reduction, Fe/SSZ-13, hydrothermal aging, FTIR, TEM, NMR, Mössbauer



1. INTRODUCTION

Selective catalytic reduction (SCR) is an important industrial catalytic process for NO_x reduction. Cu- and Fe-exchanged zeolites are the SCR catalysts of choice for the transport industry to remove NO_x generated by lean-burning diesel engines.¹ Cu/SSZ-13 and Cu/SAPO-34 are the current state-of-the-art commercial catalysts, displaying greater low-temperature activity and durability in comparison to other materials, e.g., Cu- and Fe-exchanged beta and ZSM-5 catalysts.² Hydrothermal stability and resistance to poisoning, e.g., P, S, and noble metals are the most important durability criteria of these catalysts.^{1,3–5} It has been known for some time that upon hydrothermal aging some of the isolated Cu-ions in Cu/SSZ-13 (and in Cu/zeolites in general) convert to undesirable Cu-containing species, e.g., CuO_x clusters^{6–8} and copper aluminates.^{8,9} These species do not catalyze SCR efficiently, but they are rather active in promoting side reactions including NH₃ oxidation by O₂ and N₂O formation. Consequently, aged Cu/SSZ-13 catalysts can display unsatisfactory SCR selectivities at reaction temperatures above ~300 °C.^{6,7} This is problematic because high-temperature SCR performance is extremely important during vehicle accelerations and during high-temperature maintenance events, e.g., soot combustion and SCR catalyst desulfation.¹⁰ Under such high-temperature

conditions properly formulated Fe/zeolites do offer certain advantages over Cu/zeolites, including higher SCR selectivities and lower N₂O formation.¹¹ In an effort to reap the benefits of both cations, combined Cu- and Fe-containing zeolites systems are being explored because they potentially provide optimized performance at both lower (Cu) and higher (Fe) temperatures. Therefore, continuing studies on the fundamentals of Fe/zeolite SCR catalysts are readily justified.¹²

Over the past years, Fe/beta has been identified as one of the most active and stable Fe/zeolite SCR catalysts.^{13–17} We have demonstrated recently that Fe/SSZ-13 can also be formulated to display similar activity and durability.^{12,18,19} To better understand structure–function relationships for this catalyst, we recently conducted a detailed reaction kinetics and spectroscopic study using a series of fresh, low Fe-loaded catalysts.¹² In brief, this study demonstrated that there are two key active centers in this catalyst, i.e., an isolated [Fe(OH)₂]⁺ and a dimeric [HO-Fe-O-Fe-OH]²⁺, both in charge-balancing cationic positions. It was further demonstrated that isolated [Fe(OH)₂]⁺ sites are the major low-temperature (<300 °C)

Received: December 26, 2016

Revised: February 6, 2017

Published: February 27, 2017

active centers for standard SCR ($4\text{NO} + 4\text{NH}_3 + \text{O}_2 = 4\text{N}_2 + 6\text{H}_2\text{O}$), whereas $[\text{HO-Fe-O-Fe-OH}]^{2+}$ sites are responsible for high-temperature ($\geq 300^\circ\text{C}$) SCR activity and side reactions, notably parasitic NH_3 oxidation. This catalyst also contains minority sites, i.e., isolated Fe^{2+} sites and Fe-oxide clusters and particles. Isolated Fe^{2+} sites are spectators for SCR. Fe-oxide clusters and particles may be considered as high-temperature SCR active phases. However, because these are minority sites and they catalyze NH_3 oxidation by O_2 at temperatures above 300°C , they are not key contributors in Fe/SSZ-13 SCR catalysts.

As described above, the commercial success for Cu/Chabazite catalysts is due largely to their superb hydrothermal stability. For Fe/SSZ-13, a detailed understanding of its hydrothermal stability is also of vital importance when its application potential is concerned. It has been shown recently that even at a rather low Fe loading ($\text{Fe}/\text{Al} = 0.2$), a harsh steaming treatment at 800°C for 16 h in the presence of 10% water vapor imposed no damage to the structural integrity of Fe/SSZ-13. However, a moderate drop in SCR performance was noticed, especially at low reaction temperatures.¹⁸ In the present study, we aim to further investigate changes to the zeolite framework and active sites in Fe/SSZ-13 during hydrothermal aging. This is achieved via the application of various spectroscopic and microscopic probes as detailed below.

2. EXPERIMENTAL METHODS

2.1. Catalyst Preparation. SSZ-13 material ($\text{Si}/\text{Al} = 12$) was synthesized hydrothermally using a method described in detail elsewhere.²⁰ Fe/SSZ-13 catalyst was synthesized via aqueous solution ion-exchange between SSZ-13 (in NH_4^+ form) and FeSO_4 . In brief, 2.0 g of $\text{NH}_4/\text{SSZ-13}$ and 2.0 g of $\text{FeSO}_4 \cdot 7\text{H}_2\text{O}$ were dispersed in 200 mL of deionized water for the ion-exchange process. Care was taken to facilitate Fe^{2+} ion transport into the zeolite body including (1) choosing an ion-exchange temperature of 80°C and a pH of ~ 3.0 to decrease hydration layer thickness of the Fe^{2+} ions; (2) under the protection of inert gas to prevent Fe^{2+} ion oxidation to bulky Fe(III) moieties. The as-synthesized material, after drying at 120°C and calcining in static air at 550°C for 8 h, is referred to as the fresh catalyst. Elemental analysis with inductively coupled plasma atomic emission spectroscopy (ICP-AES) at Galbraith Laboratories (Knoxville, TN, U.S.A.) indicated a Fe loading of 1.2 wt %, corresponding to a Fe/Al ratio of 0.18. More details regarding Fe/SSZ-13 formation can be found elsewhere.¹² Portions of the fresh catalyst were hydrothermally aged in air containing 10% of water vapor at 600, 700, and 800°C for 16 h. These are abbreviated as HTA samples (for example, HTA-600 represents a sample aged at 600°C).¹⁹ To facilitate Mössbauer spectroscopic measurements, another Fe/SSZ-13 sample was synthesized via ion exchange between 2.0 g of $\text{NH}_4/\text{SSZ-13}$ and Fe-57 labeled FeCl_2 ; the latter prepared by dissolving 100 mg of Fe-57 metal powder (98%, Cambridge Isotope) with stoichiometric amount of 0.1 M HCl solution at ambient temperature. This sample contained ~ 0.37 wt % Fe, and was treated hydrothermally the same way as described above.

2.2. Catalyst Characterizations. BET surface areas and micropore volumes of the fresh and aged samples were measured with a Quantachrome Autosorb-6 analyzer. Prior to analysis, the samples were dehydrated under vacuum overnight

at 250°C . Micropore volumes were determined with the t-plot method.

Powder X-ray diffraction (XRD) measurements were performed on a Philips PW3040/00 X'Pert powder X-ray diffractometer with $\text{Cu K}\alpha$ radiation ($\lambda = 1.5406 \text{ \AA}$). Data were collected with 2θ ranging from 5° to 50° using a step size of 0.02° . ^{27}Al and ^{29}Si magic angle spinning nuclear magnetic resonance (MAS NMR) analysis of the ambient fresh and HTA Fe/SSZ-13 samples was conducted on a Varian VNMRs system. Experimental details can be found elsewhere.²¹ Mössbauer spectroscopy measurements on the ambient fresh and HTA $^{57}\text{Fe}/\text{SSZ-13}$ samples were conducted at 8 K. Sample preparations, instrumentation, and measurement procedures have been detailed previously.¹⁸ NO titration FTIR was performed on a setup described in detail before.²² In brief, the setup contains a home-built transmission cell with KBr windows, a vacuum pumping system, a gas manifold, and a Bruker Vertex80 spectrometer equipped with an MCT detector. Powder samples pressed onto a tungsten mesh were treated under high vacuum ($\sim 2 \times 10^{-8}$ Torr) at 500°C for 2 h prior to cooling to ambient temperature for NO adsorption. Spectra were collected at 4 cm^{-1} resolution with an average of 256 scans against backgrounds taken with the thermally treated bare samples in order to eliminate the contribution of the intense framework vibrational features to the IR spectra.

The TEM analysis was performed with a FEI Titan 80–300 microscope operated at 300 kV. The instrument is equipped with a CEOS GmbH double-hexapole aberration corrector for the probe-forming lens, which allows for imaging with 0.1 nm resolution in scanning transmission electron microscopy mode (STEM). The images were acquired with a high-angle annular dark field (HAADF) detector with inner collection angle set to 52 mrad.

Three-dimensional nanoscale compositional characterization of Fe/SSZ-13 particles was conducted by using atom probe tomography (APT). APT is a combination of point projection microscope and time-of-flight mass spectrometer, uniquely suited to probe nanoscale compositional variations in bulk oxide materials and oxide nanoparticles.^{23,24} Needle specimens of fresh and HTA-800 Fe/SSZ-13 were prepared by a direct particle lift-out and annular milling process using an FEI Helios Nanolab 600 Dual beam FIB-SEM system, as shown in Supporting Information S-2. The APT analysis was conducted using CAMECA LEAP4000XHR atom probe tomography system equipped with a pulsed UV laser (355 nm wavelength). The pulse laser energy was kept at 100 pJ, evaporation rate was maintained at 0.005 atoms/pulse while laser pulse repeating rate was kept at 125 kHz and specimen temperature was maintained at 40 K. The APT data were reconstructed and analyzed using the IVAS software.

2.3. Reaction Measurements. NH_3 -SCR and NO/NH_3 oxidation kinetics measurements were carried out in a plug-flow reaction system equipped with an MKS MultiGas 2030 FTIR gas analyzer for reactant/product quantification. Experimental details and mathematic equations used for data analysis are given elsewhere.^{25,26} In brief, 60 mg catalysts sieved to 60–80 mesh were used for the measurements. For standard NH_3 -SCR activity testing, the feed gas contained 360 ppm of NO, 360 ppm of NH_3 , 14% O_2 , $\sim 2.5\%$ H_2O , and balanced with N_2 for a total flow rate of 300 sccm. Gas hourly space velocity (GHSV) was estimated to be $\sim 200\,000 \text{ h}^{-1}$. For NO (or NH_3) oxidation, NH_3 (or NO) was not included in the feed, while

concentrations of other gases and the total flow rate were maintained.

3. RESULTS

Structural integrity of the fresh and HTA catalysts were first studied with surface area/pore volume analysis and XRD prior to other microscopic and spectroscopic investigations. The results are shown in the [Supporting Information](#) (SI-1). Briefly, all samples display diffraction patterns only assignable to Chabazite; no discernible difference can be found among the XRD patterns of the fresh and HTA samples. Regarding surface area/pore volume changes, even the HTA-800 samples only experienced <7% of surface area/pore volume drop as compared to the fresh ones, and therefore, it is concluded that at a macroscopic level the HTA samples maintain the CHA structural integrity.

3.1. Imaging Results. Metal-exchanged zeolites can be synthesized in multiple ways, e.g., solution ion exchange, solid-state ion exchange, and one-pot methods, where aqueous solution ion exchange is most commonly practiced. It has long been realized, however, that it is difficult to form high Fe-loaded Fe/zeolites with this method,²⁷ and specifically the small pore openings in SSZ-13 result in decreased Fe²⁺ ion transport. As described above, the Fe loadings are 0.37 and 1.2%, corresponding to Fe/Al ratios of ~0.06 and 0.18 for our fresh catalysts. Fortunately, a high Fe loading is not required for NH₃-SCR applications.^{28,29} In our previous study, by means of CO/NO titration and quantification with UV-vis and Mössbauer spectroscopies, it has been concluded that the majority of Fe is in atomically dispersed states (monomeric and dimeric ions) at such low ion-exchange levels.¹² Next, TEM imaging was applied to further probe Fe dispersion in the 1.20% Fe-loaded samples. [Figure 1a](#) presents TEM image of a portion of a fresh Fe/SSZ-13 particle (scale bar 5 nm). This image is featureless; no accumulation of Fe-oxide clusters can be identified. EDS of the image (not shown) indicated the

presence of Fe, thus providing direct evidence on Fe-ion migration into the zeolite body. Occasionally, however, Fe enrichment at the zeolite particle surface is observed. This phenomenon is highlighted with a dashed oval shown in [Figure 1b](#) (scale bar 20 nm). At a much larger scale, as displayed in [Figure 1c](#) (scale bar 150 nm), needle-shaped particles are also observed (highlighted with dashed cycles). For these needle-shaped particles, only O and Fe are detected via EDS demonstrating that these are Fe-oxide particles. These images demonstrate clearly that Fe is not uniformly dispersed in fresh Fe/SSZ-13. One possible reason is that during ion exchange, or the subsequent washing, some Fe²⁺ ions are oxidized to Fe(III) species, e.g., FeOOH, which is known to be too bulky to penetrate into zeolite pores. These species then accumulate at the zeolite surface, or form free needle-shaped Fe-oxide particles during calcination. Note that these nonideal phases only comprise a small portion of Fe in Fe/SSZ-13; the majority of Fe is still properly exchanged into the zeolite.

Atom probe tomography (APT) was used to further probe whether the portion of Fe-ions exchanged into SSZ-13 particles is uniform dispersed. The APT sample preparation is detailed in [Supporting Information](#) (SI-2). As shown in [Figure 2](#), the

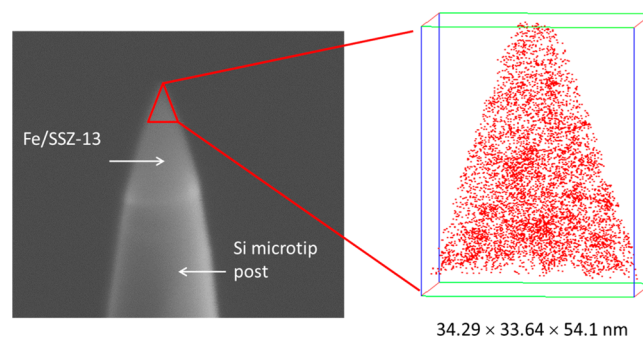


Figure 2. SEM image of a fresh Fe/SSZ-13 sample (1.20% Fe loading) + Si tip assembly, and atom probe tomography (APT) analysis for Fe distribution. APT size is marked adjacent to the image.

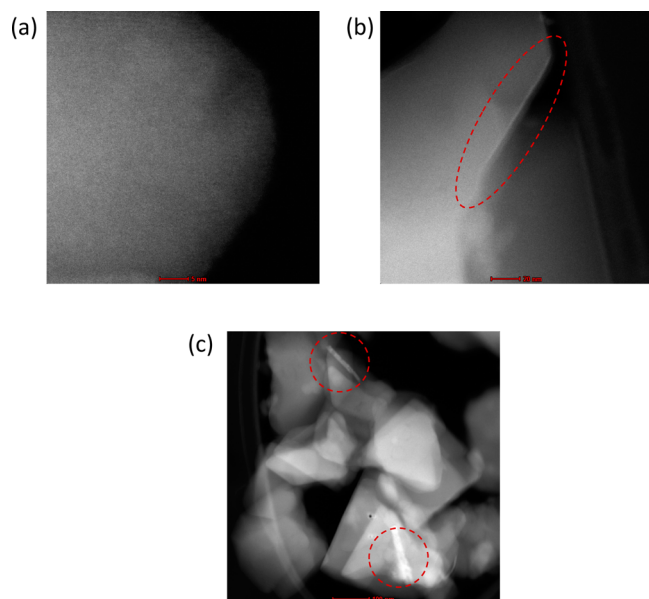


Figure 1. TEM images of fresh Fe/SSZ-13 catalyst (1.20% Fe loading): (a) representative individual particles; (b) occasional individual particles with Fe enrichment at particle edges; (c) larger-scale image with needle-shaped Fe-oxide particles.

portion of Fe exchanged into SSZ-13 particles appears to be rather uniformly dispersed. This is consistent with the assumed random distribution of framework Al and the fact that these Fe-ions stay in extra-framework cationic sites. However, this conclusion should be treated with caution because the APT sampled area is much smaller than individual SSZ-13 particles (~1.3 μm diameter on average).

[Figure 3a](#) presents TEM image of a portion of a representative HTA-800 particle (scale bar 10 nm). In comparison to [Figure 1a](#), it is obvious that while the fresh catalyst is essentially featureless, uniformly dispersed spots ~1–2 nm in size, lighter than the zeolite matrix, were observed for the HTA-800 sample, demonstrating formation of clusters denser than the zeolite matrix. However, because of their small sizes, EDS was not applicable to probe their compositions. Moreover, from this image alone, it is not possible to determine whether these clusters are located on the surface, or in the bulk. Note also that Fe enrichment at particle edges is no longer observable on any of the particles examined. At a larger scale (scale bar 100 nm), as shown in [Figure 3b](#), needle-shaped particles are still present (highlighted with dashed cycles). [Figure 3c](#) presents EDS of the SSZ-13 matrix (upper panel) and the needle-shaped particles (lower panel). The SSZ-13 matrix spectrum is expected as it is composed of O, Si, Al, and

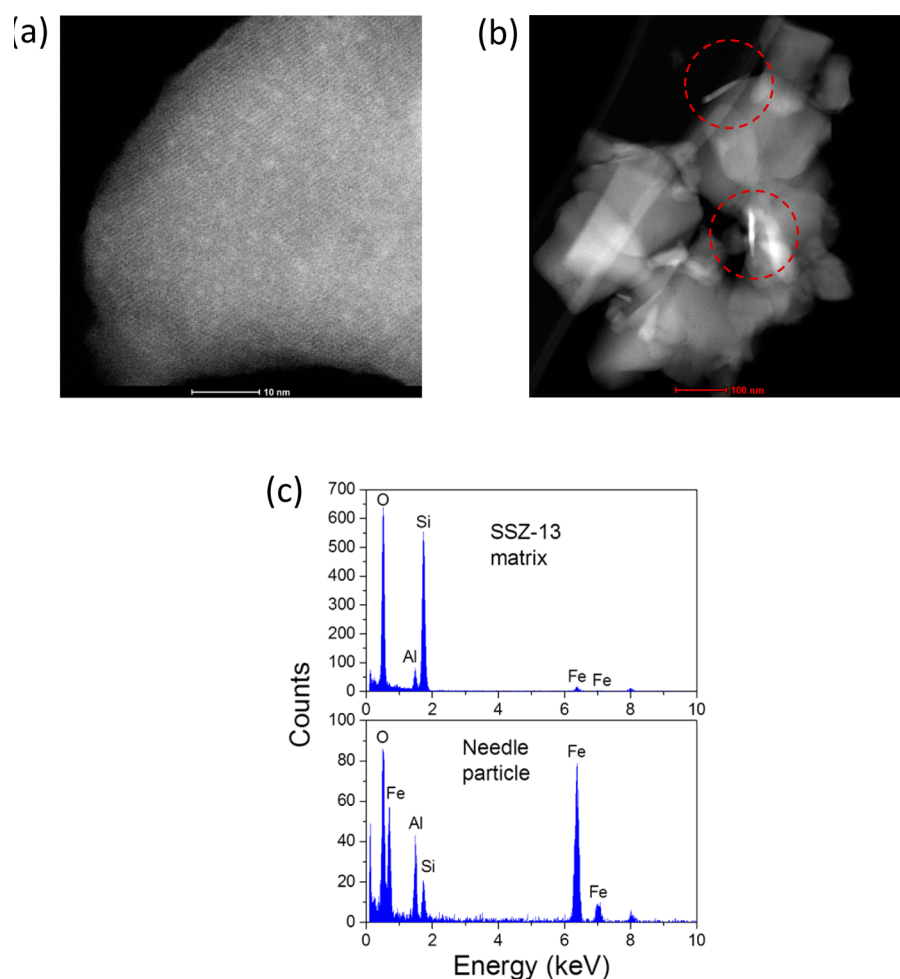


Figure 3. (a) TEM image of a representative HTA-800 Fe/SSZ-13 catalyst (1.20% Fe loading) demonstrating formation of Fe-oxide aggregates; (b) larger-scale image displaying the preservation of needle-shaped particles; (c) EDS of the SSZ-13 matrix (upper panel) and the needle-shaped particles (lower panel). Note that the weak Cu signals at ~ 8 keV come from the TEM grid rather than the catalyst.

detectable amounts of Fe. Note specifically that the needle-shaped particles in fresh samples are Fe-oxides, whereas in the HTA-800 sample they are enriched in Al, resulting from apparent conversion to Fe-aluminate-like species during aging. As can be seen in the APT image of an HTA-800 sample (SI-3), Fe within the CHA particle remains uniformly dispersed, and qualitatively, this image resembles that of the fresh sample. Note that no Fe clusters in the nanometer range are observed, suggesting that the clusters seen in Figure 3a are located on the zeolite surface and are therefore susceptible to being removed during the APT specimen preparation (SI-2). Again, the small sampling size for APT precludes a firm conclusion.

3.2. Spectroscopy Results. As described above, no apparent change in the macroscopic structure of the Fe/SSZ-13 catalyst was observed prior to and after hydrothermal aging. To investigate changes in the catalyst structure at an atomic level and to elucidate the nature of the Fe sites, spectroscopic methods were applied to the fresh and HTA samples.

^{27}Al and ^{29}Si solid-state MAS NMR was used to probe the structure of fresh and HTA SSZ-13 catalysts. As shown in Figure 4a, the fresh, 1.2% Fe-loaded catalyst (bottom spectrum) is characterized by a narrow ^{27}Al resonance at ~ 59 ppm assigned to tetrahedral Al within the framework. Nonframework, octahedral Al (at ~ 0 ppm) comprises $<5\%$ of the Al in this catalyst. Upon hydrothermal aging, two key findings are

worth noting: (1) framework Al signal intensity decreases monotonically with increasing aging temperature; for the aged samples, framework Al signals also broaden considerably in comparison to the fresh sample. (2) The disappearance of framework Al is not accompanied by the expected increase in extraframework Al signal intensity. The detectable framework Al remaining in the HTA samples were normalized against that of the fresh catalyst, and the results are displayed in Figure 4a adjacent to the corresponding spectra. The ^{27}Al NMR results demonstrate extensive dealumination in hydrothermal aging, and the extent increases with increasing temperature. However, the departed Al species appear to be NMR silent. More details will be discussed below.

Figure 4b presents the corresponding ^{29}Si NMR results. The fresh catalyst contains two framework tetrahedral Si (Q4) features: one at -105 ppm assigned to tetrahedral Si with three Si and one Al neighbors (i.e., $\text{Si}(\text{OSi})_3(\text{OAl})$) and one at -111 ppm assigned to tetrahedral Si with four Si neighbors (i.e., $\text{Si}(\text{OSi})_4$).³⁰ With increasing hydrothermal aging temperature, the -105 ppm resonance gradually diminishes, and the -111 ppm resonance intensifies and narrows. Note that the disappearance of $\text{Si}(\text{OSi})_3(\text{OAl})$ during hydrothermal aging is fully consistent with catalyst dealumination found in Figure 4a. It is interesting, however, that sample dealumination is not accompanied by the appearance of Q2 and Q3 features (i.e.,

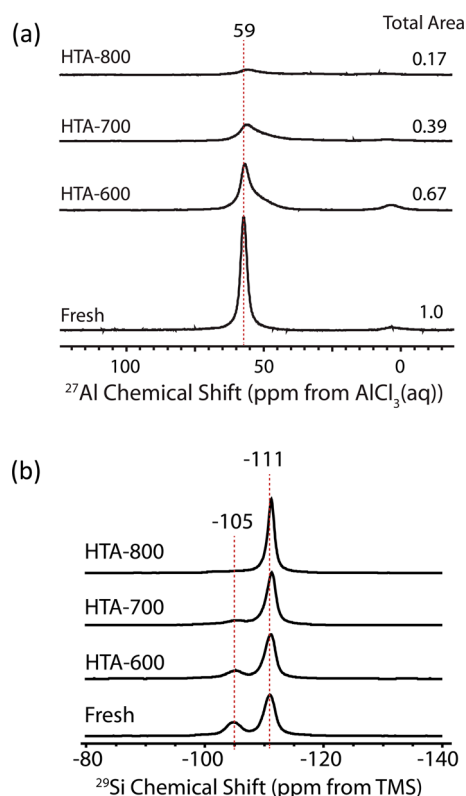


Figure 4. (a) Solid-state ^{27}Al -NMR spectra of the fresh and HTA Fe/SSZ-13 samples (1.20% Fe loading); (b) the corresponding ^{29}Si NMR spectra.

$\text{Si}(\text{OSi})_2(\text{OH})_2$ and $\text{Si}(\text{OSi})_3(\text{OH})$,³⁰ expected at ~ -90 and -100 ppm, respectively, as it is well-known that zeolite dealumination is achieved via sequential hydrolysis of $-\text{Si}-\text{O}-\text{Al}-$ linkages (i.e., $-\text{Si}-\text{O}-\text{Al}- + \text{H}_2\text{O} \rightarrow -\text{Si}-\text{OH} + \text{HO}-\text{Al}-$). Rather, signal intensity for $\text{Si}(\text{OSi})_4$ increases with increasing hydrothermal aging temperature. This strongly suggests that defects created via dealumination are subsequently “self-healed” to sustain structural integrity of SSZ-13 during aging. Again, this will be discussed further below.

We have shown recently that cryogenic temperature Mössbauer spectroscopy is by far the most accurate method in quantifying all possible Fe moieties in Fe/SSZ-13.¹² In fresh samples, three components have been observed: (1) (super)paramagnetic Fe(II) designated as Fe(II)-P, which is assigned to isolated Fe^{2+} ions; (2) (super)paramagnetic Fe(III) designated as Fe(III)-P, which is attributed to $[\text{HO}-\text{Fe}-\text{O}-\text{Fe}-\text{OH}]^{2+}$ dimers; and (3) ferromagnetic and antiferromagnetic Fe(III), collectively designated as Fe(III)-M, which is assigned to a mixture of isolated $[\text{Fe}(\text{OH})_2]^+$ and Fe-oxide clusters and particles. At low Fe loadings, isolated $[\text{Fe}(\text{OH})_2]^+$ is the major component of Fe(III)-M.¹² Note that at cryogenic temperatures, Fe(II)-P and Fe(III)-P spectra display a doublet pattern and Fe(III)-M spectra display a sextet pattern making qualitative identifications relatively straightforward. Quantification, on the other hand, requires extensive data simulation.

Fe species in fresh and HTA samples were quantified by experimental Mössbauer coupled to simulations utilizing the Voigt-based fitting model and elemental multiplet Lorentzian half width at half-maximum (hwhm) was fixed at 0.097 mm/sec. Note that these samples have an Fe loading of $\sim 0.37\%$, lower than samples used for other analyses shown above

($\sim 1.2\%$). The experimental data with the fitted curves are depicted in Figure 5, and the simulation results are presented in

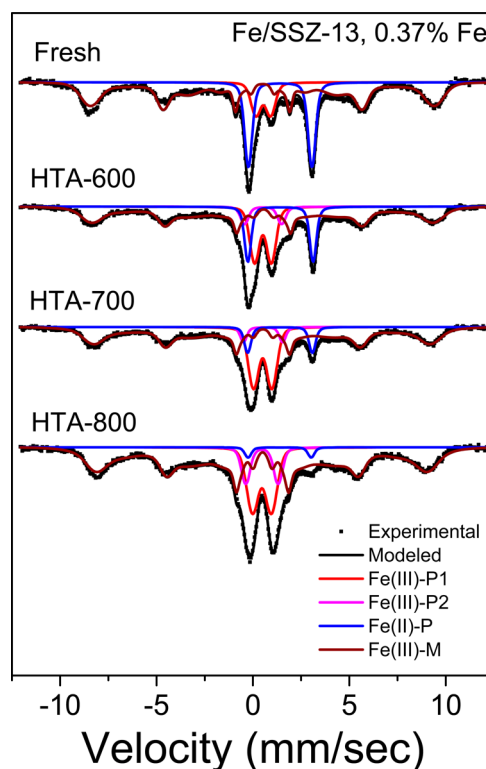


Figure 5. Experimental and simulated Mössbauer results for fresh and HTA Fe/SSZ-13 samples (0.37% Fe loading) measured at 7 K. Detailed simulation results are shown in Table 1.

Table 1. A few key findings are worth addressing: (1) The amounts of Fe(III)-M (isolated $[\text{Fe}(\text{OH})_2]^+$ (major) and Fe-oxides (minor)) stay at ~ 60 wt % in the fresh and HTA-600/700 samples. Only in the HTA-800 sample does the value increase to 68%. This indicates that interconversion between paramagnetic and magnetic Fe species is insignificant during hydrothermal aging, especially at aging temperatures ≤ 700 °C. (2) The amounts of Fe(II)-P (i.e., isolated Fe^{2+} species) decrease monotonically with increasing hydrothermal aging temperature. For example, 26.4% of Fe stays as isolated Fe^{2+} in the fresh catalyst; however, its content drops to 2.0% in the HTA-800 sample. (3) In the fresh sample, only one Fe(III)-P component is required for satisfactory data simulation. However, in the aged samples, two such components, designated as Fe(III)-P1 and Fe(III)-P2, are needed. High QS values ranging from 0.76 to 2.4 mm/s are typical for dinuclear Fe(III) complexes.³¹ Based on the QS values shown in Table 1, both are assigned to $[\text{HO}-\text{Fe}-\text{O}-\text{Fe}-\text{OH}]^{2+}$ dimers, yet with somewhat different local environments for the Fe nuclei that are most likely representative of different locations within the zeolite. Data shown in Table 1 demonstrate a nearly net conversion of isolated Fe^{2+} ions to $[\text{HO}-\text{Fe}-\text{O}-\text{Fe}-\text{OH}]^{2+}$ dimers during hydrothermal aging. It is also important to note from Table 1 that the average hyperfine magnetic field for the sextets decreases with increasing HTA temperature, most notably for the HTA-800 sample. This could be due to increasing incorporation of Al into the Fe-oxide phases (i.e., magnetic dilution). This notion is fully in line with EDS and ^{27}Al NMR observations; more details will be given below.

Table 1. Simulated Key Mössbauer Parameters and Estimated Percentages of Various Fe Components in the Fresh and HTA Fe/SSZ-13 Samples (0.37% Fe) Measured at 8 K

sample	component	center shift (CS, mm/s)	quadrupole splitting (QS, mm/s)	quadrupole shift (ϵ , mm/s)	hyperfine magnetic field (HF, Tesla)	percentage (%)
fresh	Fe(III)-P	0.53	0.77	—	—	12.4
	Fe(II)-P	1.41	3.29	—	—	26.4
	Fe(III)-M	0.49	—	−0.01	44.97	61.2
HTA-600	Fe(III)-P1	0.52	0.87	—	—	21.3
	Fe(III)-P2	0.53	1.9	—	—	5.8
	Fe(II)-P	1.43	3.38	—	—	15.7
HTA-700	Fe(III)-M	0.52	—	−0.03	42.02	57.2
	Fe(III)-P1	0.51	0.95	—	—	26.6
	Fe(III)-P2	0.53	2.03	—	—	4.5
HTA-800	Fe(II)-P	1.40	3.35	—	—	7.6
	Fe(III)-M	0.49	—	0.03	42.7	61.4
	Fe(III)-P1	0.47	0.99	—	—	21.0
	Fe(III)-P2	0.47	1.68	—	—	9.0
	Fe(II)-P	1.38	3.27	—	—	2.0
	Fe(III)-M	0.48	—	−0.02	39.8	68.0

We have shown recently that CO/NO chemisorption FTIR can be used to probe the location of Fe ions in Fe/SSZ-13.^{18,22} At ambient temperatures, NO selectively adsorbs on Fe(II) sites and forms mono- and multinitrosyls depending on Fe(II) positioning, thus providing useful information on active site locations. Because NO only interacts extremely weakly with Fe(III) sites, a sample reduction treatment, e.g., annealing in vacuum for “self-reduction” is required. However, the extent for such self-reduction is not known, and potential Fe-ion migration is possible during such reduction. Therefore, this technique is incapable of titrating all of the Fe-ions and cannot provide Fe-ion positioning information for hydrated or oxidized samples. Yet, as will be shown below, important structural information can still be derived.

Figure 6a presents IR spectra of the N–O stretching vibrational region at chemisorption-gas phase equilibrium where the gas-phase NO pressure is ~ 0.4 Torr. On the 1.2% Fe-loaded fresh sample, multiple ν_{NO} bands are observed. These can be rather accurately assigned: the 1885 cm^{-1} band due to mononitrosyl adsorbed on Fe(II) ions located in windows of six-membered ring (6MR) of Chabazite and the 1850/1772 and the 1916/1810/1797 cm^{-1} band groups are attributed to dinitrosyl (Fe(II)-(NO)_2) and trinitrosyl (Fe(II)-(NO)_3) adsorbed on Fe(II) ions located in 8MR windows, respectively.²² The 1902 and 1836 cm^{-1} bands can be assigned to gas-phase NO (including the amount physically trapped in Chabazite channels and cages). For the HTA samples, a general trend is that the overall signal intensities decrease with increasing hydrothermal aging temperature, indicative of availability decrease for Fe(II) sites. This is specifically the case for the HTA-800 sample. For the HTA-600/700 samples, new bands appear in the 1865–1875 cm^{-1} range. As suggested earlier, these are assigned to NO adsorbed on surface Fe(II) of FeOx (including FeAlOx) clusters,^{18,32} indicating Fe-ion clustering occurs as low as 600 °C.

Figure 6b presents the corresponding spectra after evacuating the IR cell. The gas-phase NO bands and the majority of trinitrosyl bands disappear rapidly. For the fresh sample in particular, this is accompanied by a signal enhancement for dinitrosyl indicating trinitrosyl conversion to dinitrosyl by losing one NO ligand. Note that for Fe(II)-(NO)_2 , the asymmetric feature at 1772 cm^{-1} is stronger than the symmetric

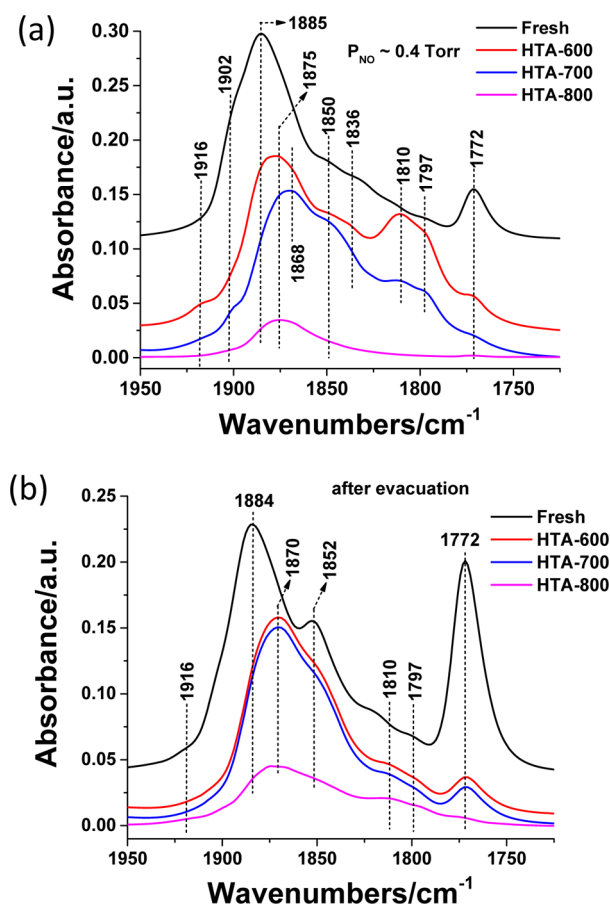


Figure 6. IR spectra obtained after exposure of fresh and HTA Fe/SSZ-13 samples to NO at ambient temperature: (a) in equilibrium with ~ 0.4 Torr NO in the gas phase, (b) after NO evacuation. The samples were annealed in vacuum at 500 °C for 2 h prior to IR measurements.

band at 1852 cm^{-1} as clearly shown on the fresh sample. However, for the HTA samples, the 1852 cm^{-1} band is stronger, indicating contribution also from NO adsorbed on surface Fe(II) of FeOx clusters.^{18,32}

3.3. Reaction Results. Catalytic performance of fresh and aged Fe/SSZ-13 samples were tested using standard SCR, NH_3

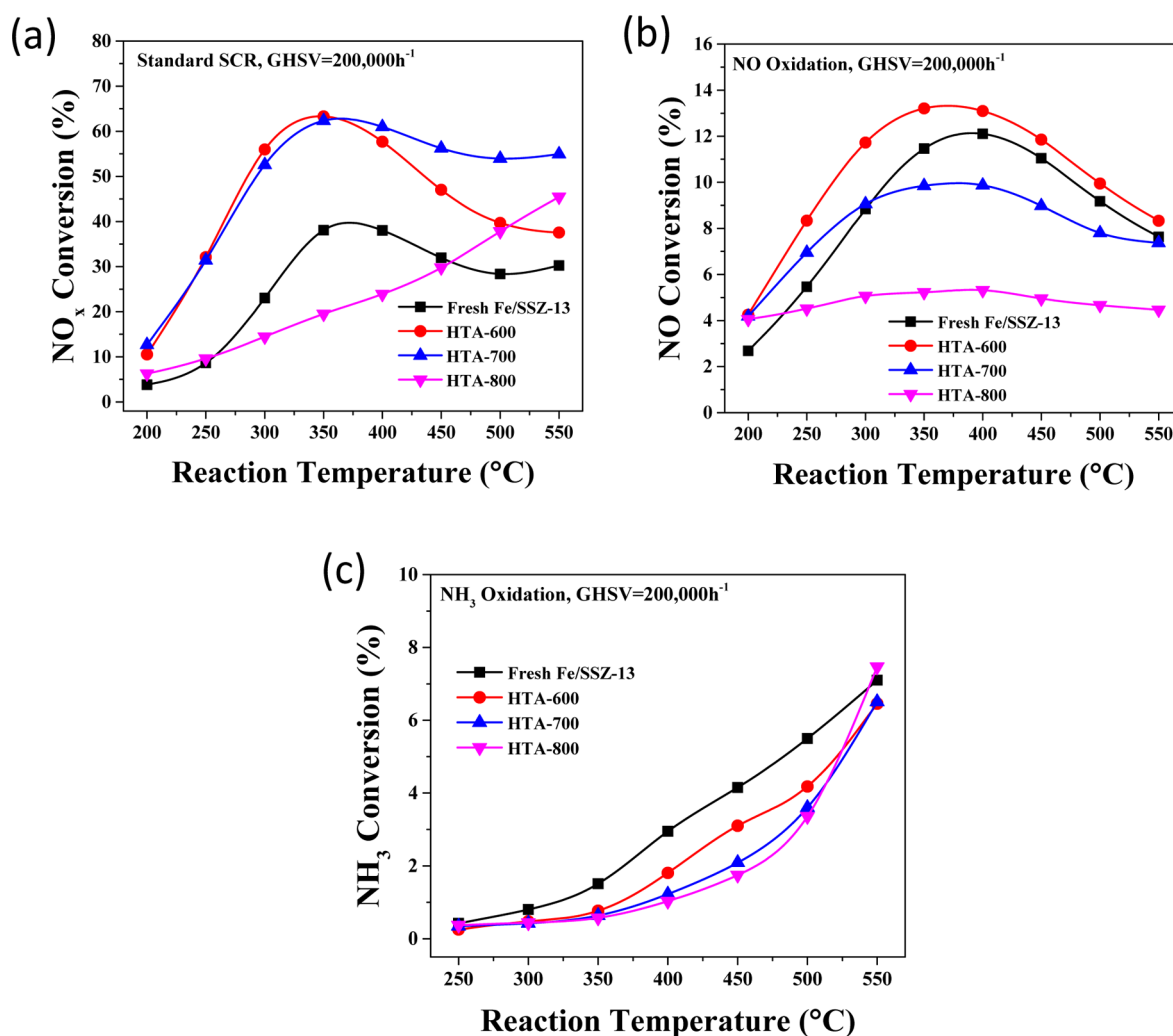


Figure 7. (a) NO_x conversion as a function of reaction temperature in standard SCR over fresh and HTA Fe/SSZ-13 samples with Si/Al = 12 and Fe loading of 0.37%. Reactant feed contains 350 ppm of NH₃, 14% O₂, 2.5% H₂O balanced with N₂ at a GHSV of 200 000 h⁻¹. (b) NO conversion versus temperature for NO oxidation over the same catalysts. (c) NH₃ conversion versus temperature for NH₃ oxidation over the same catalysts. For the latter two reactions, NH₃ (or NO) was not included in the gas feed; other components maintain the same as in standard SCR.

oxidation ($4\text{NH}_3 + 3\text{O}_2 = 2\text{N}_2 + 6\text{H}_2\text{O}$) and NO oxidation ($2\text{NO} + \text{O}_2 = 2\text{NO}_2$) reactions. According to our previous study, $[\text{Fe}(\text{OH})_2]^+$ and $[\text{HO-Fe-O-Fe-OH}]^{2+}$ are the main contributors to SCR, NO oxidation is catalyzed mainly by $[\text{HO-Fe-O-Fe-OH}]^{2+}$ sites, and NH₃ oxidation is predominately carried out on minor Fe-oxide sites.¹² Therefore, these reactions collectively are very informative in elucidating changes to the nature of Fe sites in hydrothermal aging. However, the SCR process is complex due to involvement of redox of active centers, activation/interaction of multiple components (NO_x, NH₃ and O₂), and strong temperature dependence.¹ In the present study, we intend to only provide qualitative analyses of these reaction results based on conversion–temperature curves collected under industrial relevant space velocities ($\sim 200\,000\text{ h}^{-1}$ for powder catalysts).

Reaction results on the 1.2% Fe-loaded samples have been published elsewhere.¹⁹ These data are again provided in Supporting Information (SI-4). Results on the 0.37% Fe-loaded samples (used for Mössbauer studies) are presented in Figure 7. These results resemble data shown in SI-4, but with lower conversions due to lower active site concentrations. As shown in Figure 7a, SCR performance of the HTA-600 sample

substantially outperforms the fresh sample; the HTA-700 sample maintains similar performance as the HTA-600 sample $\leq 400\text{ }^\circ\text{C}$ and outperforms the latter at higher temperatures. Note that these three samples display their best performance between 350 and 400 °C. The HTA-800 sample behaves very differently, where NO_x conversions increase monotonically with increasing temperature. This indicates that the nature of active centers and/or reaction mechanisms for the HTA-800 sample is quite different from the other samples. Figure 7b displays NO oxidation reaction results. For the fresh, HTA-600 and -700 samples, the highest NO conversions also appear between 350 and 400 °C. This suggests some positive correlation between SCR and NO oxidation. However, “gas phase” NO₂ formation is clearly not a rate-limiting step for SCR because SCR rates are apparently faster than NO oxidation at any reaction temperature. Again, the HTA-800 sample behaves differently also in NO oxidation, where NO conversions are lower than the other samples and do not appear to vary substantially with temperature. Figure 7c presents NH₃ oxidation results. All four samples show weak activity toward NH₃ oxidation, consistent with the low contents of Fe-oxide species in these samples. Below $\sim 500\text{ }^\circ\text{C}$, NH₃ conversions

decrease with increasing aging temperature, suggesting that NH_3 storage capacity (which also decreases with increasing aging temperature) plays a positive role in this reaction.¹⁹ At a reaction temperature of 550 °C, the HTA-800 sample exhibits unusual behavior and displays activity even slightly higher than the fresh sample. In standard SCR, N_2O formation is insignificant (≤ 1 ppm) under any reaction condition, consistent with the fact that Fe/zeolites are less selective than Cu/zeolites in N_2O formation. In NH_3 oxidation at temperatures below 500 °C, no N_2O and NO formation can be detected. At 500 and 550 °C, a few ppms of NO are detected (Figure S4d), but N_2O is still undetectable, demonstrating that his reaction is highly selective toward N_2 formation.

4. DISCUSSION

The aims of the present study are the following: (1) to investigate rearrangement of the catalyst components, including the Fe active phases and the SSZ-13 support, during hydrothermal aging; and (2) to establish a thorough understanding of how these structural changes affect the catalytic performance and stability of Fe/SSZ-13.

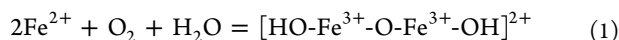
A few conclusions are readily derived from TEM imaging and EDS analysis. First, large-scale Fe enrichment on the fresh zeolite external surface (Figure 1b) has not been observed on any of the hydrothermally aged samples, demonstrating that during aging these Fe enriched “patches” redispersed into moieties at much smaller scales. Second, Fe-ion clustering occurs during hydrothermal aging, as clearly evidenced by comparisons between Figures 1a and 3a. The 800 °C aged sample displays aggregates with sizes of 1–2 nm (Figures 3a). Assuming that these are FeOx clusters and using an O–Fe–O bond length of ~ 3 Å, these aggregates are estimated to contain tens to more than a hundred Fe atoms. From TEM imaging alone, it is not possible to determine whether these are located inside zeolite channels/pores, or deposited on external surfaces. It is interesting to note that these clusters have sizes on the same order as Chabazite unit cells ($13.5 \times 13.5 \times 15$ Å³).³³ In order to maintain SSZ-13 structural integrity as evidenced from XRD (Figure S1), it is more likely that these clusters primarily locate at zeolite particle external surfaces. Note that this is consistent with APT analysis of an HTA-800 particle where Fe-containing clusters in the nanometer range are not found in the bulk of the sample (SI-3). However, we cannot preclude the presence of such clusters in the catalyst bulk because the APT sampled volume may not be entirely representative. In this case, some new channels must form inside individual particles to accommodate these clusters. It will be shown below that this notion is consistent with ²⁹Si NMR characterizations (Figure 4b). Third, needle-shaped particles in the fresh catalysts (Figure 1c) are preserved during hydrothermal aging (Figure 3b); however, their chemical composition changed dramatically. In the fresh catalysts these are Fe-oxides, while in the HTA samples, they become enriched in Al (Figure 3c, lower panel). Fickel et al. speculated that $\text{Al}(\text{OH})_3$, the product of zeolite dealumination, cannot exit SSZ-13 pores because its kinetic diameter (~ 5 Å) is larger than the Chabazite pore openings (~ 3.8 Å).³⁴ Our findings here do not support this assertion; detached Al moieties are indeed capable of migrating out of the Chabazite pores, otherwise the Al enrichment of the needle-shaped Fe-oxide particles cannot be explained. One possible explanation is that the Al species migrating out of the Chabazite pores is not $\text{Al}(\text{OH})_3$, but moieties with smaller kinetic diameters, e.g., $\text{AlO}(\text{OH})$. Under high-temperature hydro-

thermal aging conditions, the presence of $\text{AlO}(\text{OH})/\text{Al}(\text{OH})_3$ equilibrium may very well exist. Furthermore, Al enrichment in Fe-oxides brings about another topic worth discussing, that is, what chemical phase(s) forms during this process. It has been known from Fe–Al–O and Cu–Al–O phase equilibrium studies that for spinel structures (AB_2O_4), CuAl_2O_4 can form readily under destructive hydrothermal aging conditions of Cu/zeolites, while FeAl_2O_4 cannot.^{35,36} However, even for the case of Cu/zeolites, there has been no evidence on the formation of the stoichiometric CuAl_2O_4 spinel phase.⁹ In the present study, it is clearly shown that Al enrichment in Fe-oxides does occur under hydrothermal aging conditions. On the basis of prior phase equilibrium studies, it is certain that a spinel phase is not formed. Rather, one expects formation of Fe-aluminate-like species, or simply Fe–Al mixed oxides in this case. More generally, for both Cu and Fe/zeolites, it can be said that Cu(Fe)–Al mixed oxides form during hydrothermal aging. These phases are structurally and compositionally less determined, even though they have some resemblance to stoichiometric Cu(Fe)–aluminates.

As shown above, during hydrothermal aging, Al enrichment in Fe-oxides is evidenced from EDS analysis of needle-shaped Fe-oxide particles present already in the fresh catalyst. For the Fe-oxide clusters that form during hydrothermal aging (Figure 3a), their small sizes make precise compositional analysis based on EDS impossible. However, there is no reason to preclude Al incorporation into these clusters. As will be discussed below, on the basis of Mössbauer spectroscopy and NO titration FTIR, strong evidence exists for Al enrichment in these clusters as well.

More details on the transformation of Fe-containing moieties during hydrothermal aging are derived from Mössbauer spectroscopy (Figure 5). Prior to detailed discussions, we note that the assignment of Fe(II)–P to isolated Fe^{2+} ions is based on its high center shift of ~ 1.42 mm/s^{31,37,38} and the fact that this species is barely detectable at ambient temperatures because of its nonrecoil free (i.e., mobile) nature.¹² The attribution of the Fe(III)–P to dinuclear $[\text{HO}-\text{Fe}-\text{O}-\text{Fe}-\text{OH}]^{2+}$ is based mainly on its high QS values, typical for dinuclear Fe^{3+} complexes.³¹ Note that in hydrothermally aged samples, two such components, Fe(III)–P1 and Fe(III)–P2, are needed for satisfactory simulation of the experimental spectra. Their QS values are different indicating that they occupy different locations in SSZ-13. However, no more details can be given at this time. The assignment of Fe(III)–M to the mixture of isolated $[\text{Fe}(\text{OH})_2]^+$ and Fe-oxides, on the other hand, was derived with the aid of other (semi)-quantification methods, specifically UV–vis spectroscopy.¹² For example, in fresh samples, the strongest UV–vis features are attributed to isolated $[\text{Fe}(\text{OH})_2]^+$, suggesting that the most abundant feature from Mössbauer, i.e., Fe(III)–M, must also contain the same species. Unfortunately, both Fe-oxide clusters and particles also display sextet signals difficult to distinguish from $[\text{Fe}(\text{OH})_2]^+$. In the present study, the Fe-57-labeled sample used for Mössbauer has a rather low Fe loading of 0.37%. Therefore, in the fresh form, this sample contains a higher percentage of isolated Fe^{2+} and a lower percentage of Fe-oxides in comparison to a higher Fe-loaded sample.¹²

The most straightforward information derived from Figure 5 is the oxidation of isolated Fe^{2+} (Fe(II)–P) to dinuclear $[\text{HO}-\text{Fe}-\text{O}-\text{Fe}-\text{OH}]^{2+}$ (Fe(III)–P) during hydrothermal aging. This chemistry can be described using the following equation:

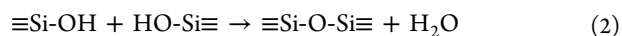


The driving force for this reaction is the particular stability of $[\text{HO}-\text{Fe}-\text{O}-\text{Fe}-\text{OH}]^{2+}$ in SSZ-13. This is evidenced by the fact that its content remains constant in all of the HTA samples (Table 1). This further indicates that Fe-ion agglomeration during aging occurs mainly to $[\text{Fe}(\text{OH})_2]^+$ species via sequential dehydroxylation condensation steps. It is also reasonable to suggest formation of larger, charge neutral Fe_2O_3 clusters at higher hydrothermal aging temperatures; and smaller, $(\text{Fe}_x\text{O}_y\text{H}_z)^{(3x-2y+z)+}$ clusters that still play charge-balancing roles at lower hydrothermal aging temperatures. Note that these moieties collectively give rise to the Fe(III)-M signal; more detailed assignments are not possible.

Fe-ion agglomeration should leave tetrahedral Al otherwise protected in the fresh catalyst by Fe-ions vulnerable for dealumination during hydrothermal aging. However, because our Fe/SSZ-13 samples are low Fe-loaded (even in the fresh form, more than ~80% of Brønsted acid sites are not ion exchanged by Fe), a simple correlation between dealumination and the extent of Fe-ion agglomeration is not readily established. As shown in Figure 4a, the amount of tetrahedral Al decreases with increasing hydrothermal aging temperature. Interestingly, in comparison to the fresh sample, only ~17% of the tetrahedral Al remains in the HTA-800 sample, essentially indicating all “free” Brønsted acid sites in the fresh sample undergo dealumination. This notion is fully consistent with NH_3 temperature-programmed desorption (NH_3 -TPD) results measured on these samples.¹⁹ However, detached Al is largely undetectable with NMR in any of the HTA samples. Aluminum nuclei may be undetectable because of extreme distortion from tetrahedral or octahedral symmetry³⁹ or proximity to paramagnetic centers (Fe(III) in this case).^{8,9} Recently, we have shown that for hydrothermally aged Na,H/SSZ-13 samples (which do not contain paramagnetic centers), detached Al adopts penta- and octahedral coordination, and it is still largely visible (~10–20% NMR “invisible”).⁴⁰ Therefore, the Al “loss” seen in Figure 4a is most likely due to the presence of proximal Fe(III). Note that in the fresh sample the presence of extra-framework Fe(III)-ions do not necessarily result in loss of Al signal. This indicates that in the hydrothermally aged samples, invisible Al stays closer to Fe atoms in Fe-oxide aggregates, e.g., on their surface and/or into their body so that Fe–O–Al bonding is realized. Besides the direct EDS evidence shown above, Mössbauer results shown in Table 1 also provide some clear evidence for Al penetration into Fe-oxides. Note that the fresh sample has a hyperfine magnetic field of ~45 T while hydrothermally aged samples show clear decrease of this parameter, specifically the HTA-800 sample (at ~40 T). This can be explained from “magnetic dilution”, i.e., Al incorporation into Fe-oxide clusters and particles.

Note from Figure 4b that with progressive hydrothermal aging, Q4 Si ($\text{Si}(\text{OSi})_3(\text{OAl})$) feature at –105 ppm gradually converts to Q4 Si ($\text{Si}(\text{OSi})_4$) at –111 ppm. According to a well-known reaction theme for zeolite dealumination, the removal of an $[\text{AlO}_4]$ tetrahedron via hydrolysis leads to formation of 4 $\equiv\text{Si}-\text{OH}$ groups surrounding a void, thus forming a so-called “hydroxyl-nest” defect.⁴¹ It is clear from Figure 4b that such defects are not present here since Q3 Si sites ($\text{Si}(\text{OSi})_3(\text{OH})$) are not detected.⁴² One possible explanation is that at high hydrothermal aging temperatures, “hydroxyl-nest” defects are unstable and neighboring $\equiv\text{Si}-\text{OH}$

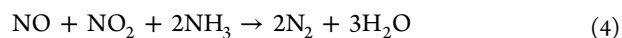
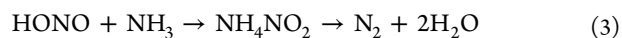
groups undergo dehydroxylation reactions to form strained siloxane bridges as described below:⁴¹



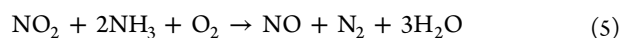
However, formation of such strained siloxane bridges would lead to broadening of the Q4 feature at –111 pm; this is not supported by spectra shown in Figure 4b. On the contrary, the fwhm of the –111 pm feature for the fresh sample is ~3.3 ppm, whereas that for the HTA-800 sample is ~2.1 ppm. Judged from this criterion, tetrahedral Si sites become even more uniformly distributed after hydrothermal aging. Alternatively, it can be argued that defects formed upon dealumination migrate and aggregate to form secondary pores or “nano cavities”.^{43,44} Even though the exact mechanisms are not known and might be very complicated, this explanation appears to be more suitable here. This follows since these secondary pores can serve as ideal locations for the nanosized (Al enriched) Fe-oxide aggregates formed during aging (Figure 3a), if some of them are located in the zeolite bulk; this arrangement does not lead to no distortion of primary pores next to such aggregates, as indicated from Figure 4b.

Formation of the (Al enriched) Fe-oxide clustered phases discussed above, at least qualitatively, can be readily confirmed via NO adsorption FTIR. As shown in Figure 6, NO vibrational bands at ~1875–1850 cm^{-1} can be assigned to NO adsorbed on their surfaces.^{18,32} This indicates that such phases form as low as 600 °C during hydrothermal aging. Because NO only titrates isolated Fe(II) sites and surface Fe(II) sites on Fe aggregates, it is also inferred from Figure 6 that Fe dispersion and/or reducibility decreases with increasing aging temperature, especially at 800 °C. Fe dispersion drop with aging is readily understood. Reducibility decreases can have the following causes: (1) Al incorporation into FeOx clusters, (2) individual $\text{Al}(\text{OH})_3$ and Fe-ion monomer/dimer interactions. For the latter, a structural model is given below that explains some of the FTIR and reaction results.

Before discussing the effects of hydrothermal aging on the catalytic performance of the Fe/SSZ-13 catalysts, it is worthwhile to briefly summarize the current understanding of active sites and reaction mechanisms of SCR over Fe/zeolites. It is generally believed that the majority of Fe-containing moieties, including isolated Fe-ion monomers, dimers, larger Fe-oxide clusters, and surface sites on Fe-oxide particles, can contribute to NH_3 -SCR.^{45–48} We suggested recently that $[\text{Fe}(\text{OH})_2]^+$ monomers and $[\text{HO}-\text{Fe}-\text{O}-\text{Fe}-\text{OH}]^{2+}$ dimers are major contributors for SCR in Fe/SSZ-13; the former is responsible for low-temperature activity and the latter is responsible for high-temperature activity and parasitic NH_3 oxidation side reactions.¹² Key issues for SCR mechanisms are (1) whether NO is activated by Fe(III) resulting in N species having a formal oxidation state of +3 (HONO , HNO_2^- , or NO^+), or to NO_2 . Note that during this step, Fe(III) is reduced to Fe(II); (2) how reduced Fe(II) centers are reoxidized to Fe(III) to regain NO activation capacity. We have suggested that $[\text{Fe}(\text{OH})_2]^+$ monomers activate NO to HONO, and dimers and larger Fe-containing entities activate NO to NO_2 .¹² These activated NOx species then react with NH_3 selectively via the following pathways:



NO₂ can also be involved in side reactions, e.g., parasitic NH₃ oxidation, via the following possible pathway:



As to active-site redox cycling, on the basis of the hypothesis that isolated reduced Fe(II) monomers cannot activate O₂,^{49,50} we further suggested that reoxidation requires participation of two reduced Fe(II) monomers. On the other hand, reduced dimers and larger Fe-oxide species can be reoxidized individually by O₂.¹²

As is clearly seen in Figures 7a and S4a, for the 0.37% and 1.20% Fe-loaded samples, respectively, the most obvious beneficial effect of hydrothermal aging is improved SCR performance of samples aged at 600 and 700 °C in comparison to the fresh sample. This improvement is in part due to the fact that SCR inactive, isolated free Fe²⁺ ions convert to SCR active, dinuclear Fe-ions during hydrothermal aging. This chemistry (described with eq 1) is well-supported by Mössbauer spectra shown in Figure 5. Like Cu²⁺ ions, isolated Fe²⁺ ions are balanced by paired Al sites in Chabazite. Progressive dealumination during hydrothermal aging destabilizes them, causing formation of more stable dinuclear [HO-Fe-O-Fe-OH]²⁺, which can in principle be stabilized by two Al sites farther apart. More evidence on Fe²⁺ ion conversion was found from the NO chemisorption results shown in Figure 6. Notably, the 1884 cm⁻¹ NO band, assigned to isolated Fe(II) species located in 6MR, has contributions from the isolated Fe²⁺ ions. The intensity of the 1884 cm⁻¹ NO band decreased with increasing aging temperature, also in line with the Mössbauer results.

The inactivity of free Fe²⁺ ions for SCR is readily understood: standard SCR proceeds via a redox mechanism, where active Fe centers must cycle between +2/+3 oxidation states. Fe sites permanently “trapped” at a +2 oxidation state do not contribute to standard SCR.⁴⁹ Free Fe²⁺ ions can survive during fresh sample calcination in air at 550 °C, demonstrating that they cannot be oxidized by O₂. This in turn suggests that they cannot be oxidized to Fe(III) moieties under standard SCR conditions (temperatures ≤550 °C, environment less oxidizing than air), a critical step for redox cycling. Therefore, the activity data coupled with Mössbauer data further corroborated this important, redox mechanism concept. The same concept can be used to understand low-temperature activity difference between Cu- and Fe/zeolites in standard SCR. The much lower activity for Fe/zeolites is due to facile Fe(III) reduction to Fe(II) by NH₃, such that Fe(III)/Fe(II) redox cycling is much more difficult than Cu(II)/Cu(I) redox cycling at low temperatures.¹¹

The SCR performance enhancement after hydrothermal aging for Fe/SSZ-13 is not seen for Fe/ZSM-5³⁹ and Fe/beta¹⁹ catalysts. The latter materials lack structural rigidity as compared to SSZ-13; therefore, hydrothermal aging at 600 °C and above always leads to a certain degree of deactivation. The loss of active centers from deactivation makes these materials nonoptimal for studying catalytic properties definitively assigned to changes in active centers. However, the chemical complexity of SCR makes definitive structure–function relationships difficult to discern even in materials that maintain their active centers, such as Fe/SSZ-13. To gain a better understanding of the effects of hydrothermal aging to SCR kinetics, in the following reaction, rates were treated using the first-order kinetic equation, i.e., $r = \frac{F}{W}(-\ln(1 - x))$ where

F is the NO flow rate (moles of NO per s), w the mass of the catalyst (g), and x the NO conversion. Thereafter, Arrhenius equation, $k = \frac{r}{[\text{NO}]_0} = Ae^{-E_a/RT}$, was used for the calculations of preexponential factors (A) and apparent activation energies (E_a), where k is the rate constant, and $[\text{NO}]_0$ the molar concentration of NO in the feed.⁵¹ The low-temperature, linear-regime Arrhenius plots are displayed in SI-5, and the corresponding kinetics parameters obtained are tabulated in Table 2. For the 1.20% Fe-loaded samples, prefactors decrease

Table 2. Preexponential Factor (A) and Apparent Activation Energy (E_a) Values Obtained via Analysis of the Low-Temperature Standard SCR Results Using Arrhenius

$$\text{Equation } k = \frac{r}{[\text{NO}]_0} = Ae^{-E_a/RT}$$

sample		A (s ⁻¹)	E_a (kJ/mol)
0.37% Fe/SSZ-13	fresh	210	48.0
	HTA-600	290	43.1
	HTA-700	75	37.4
	HTA-800	0.3	19.4
1.20% Fe/SSZ-13	fresh	1500	52.9
	HTA-600	1100	48.4
	HTA-700	450	43.4
	HTA-800	140	43.8

with increasing aging temperature, indicating progressive loss of active centers. Apparent activation energies slightly decrease with aging, indicating some but not dramatic changes to the nature of active centers. For the 0.37% Fe-loaded samples, the HTA-800 sample behaves very abnormally in terms of both prefactor and apparent activation energy values, indicating that active sites in this sample are drastically different from others. However, as shown in Figure 5 and Table 1, at least for dimeric sites, this sample is not significantly different from other samples. Possible explanations will be given below.

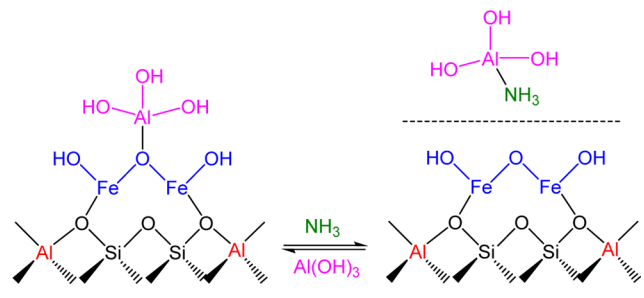
From the catalyst characterizations shown above, specifically from Mössbauer spectroscopy and TEM imaging, the amounts of Fe(III)-dimers remain approximately constant among HTA samples, whereas the amounts of Fe(III)-monomers decrease and the amounts of Fe-oxide clusters increase with aging temperature. As seen in Figure 7b, NO oxidation ability does not always increase with increasing hydrothermal aging temperature; the HTA-600 sample becomes more active than the fresh sample as expected, yet an apparent activity decline is found for the HTA-700 sample. For the HTA-800 catalyst, this decline becomes even more dramatic. This can be attributed to an “Al poisoning” effect. For Fe-oxides, both hyperfine magnetic field analysis from Mössbauer and EDS analysis indicate Al incorporation into Fe-oxides. This may alter catalytic activity for oxidation in a negative way. Indeed, to the best of our knowledge, iron aluminate-like materials are not known as efficient oxidation catalysts. For [HO-Fe-O-Fe-OH]²⁺ dimers, although their contents do not decline with increasing hydrothermal aging temperature, Al poisoning can still occur when detached Al(OH)₃ interacts strongly with the dimeric centers. This effect is schematically shown below:

According to this scheme, detached, free Al(OH)₃ species can poison a dimeric active site via a Lewis acid–base interaction mechanism, i.e., bonding between Al and the extra lattice oxygen, thus inhibiting its oxidation catalysis and redox cycling. This notion is again partly supported by NO titration spectra shown in Figure 6. Notably, the HTA samples become

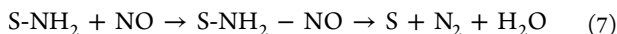
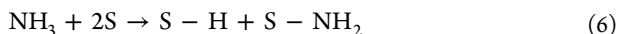
more difficult to reduce during the high-temperature “auto-reduction” treatment, also indicating increased redox barriers.

As also shown in Scheme 1, in the presence of strong Lewis base species, e.g., NH_3 , this inhibition effect can be mitigated.

Scheme 1. $\text{Al}(\text{OH})_3$ Poisoning Effect on a $[\text{HO-Fe-O-Fe-OH}]^{2+}$ Dimeric Active Site



Therefore, this scheme appears to be able to reconcile the SCR and NO oxidation activity differences between HTA-600 and 700 samples, that is, the HTA-600 sample is more active in NO oxidation because it is less inhibited by $\text{Al}(\text{OH})_3$, yet in terms of SCR, both samples are essentially equally active because this inhibition effect is removed by NH_3 (Figures 7 and S4). For the HTA-800 sample, it is possible that dimeric sites are poisoned by more than one $\text{Al}(\text{OH})_3$ units; therefore, extra lattice oxygen is no longer liberated even in the presence of NH_3 (Figure 7c). For this catalyst, however, a high-temperature SCR reaction channel appears to come into play (Figure 7a), where key reactions can be described as follows:



In this case, the active sites (S) become Fe-oxides with Al incorporation (or iron aluminate-like species). This assignment is consistent with the fact that the 0.37% Fe-loaded HTA-800 sample has active sites very different from other samples (Table 2). Note that Al incorporation into Fe-oxides is indispensable in this case to lower oxidation potential for Fe-oxides to favor the SCR pathway. Otherwise, it is expected that $\text{S} - \text{NH}_2$ intermediates will be unselectively oxidized by O_2 . Note also that the 1.20% Fe-loaded HTA-800 sample behave more similarly to fresh and HTA-600/700 samples than the 0.37% Fe-loaded HTA-800 sample, indicating that this sample is modified by detached $\text{Al}(\text{OH})_3$ species less dramatically.

A long-standing question with SCR mechanisms is whether NO_2 formation is an essential (even rate-limiting) step in standard SCR,^{1,52} the paradigm holding that NO_2 formation is indispensable has been challenged recently.^{53,54} Recently, we suggested that for Fe sites highly active in NO oxidation to NO_2 (e.g., dimers and clusters), there is a correlation between NO_2 formation and SCR. However, for monomeric sites, these two reactions are not related.¹² In the present study, by comparing SCR and NO_2 formation curves displayed in Figures 6 and S4, we note again that different Fe sites respond very differently toward zeolite dealumination, thus further complicating the correlation between these two chemistries. Aside from the nature of Fe active centers, residual Brønsted acidity of the zeolite also plays important roles in SCR because ethis largely determines ammonia storage capacity. Ammonia has longer residence time (i.e., higher reaction probability) in catalysts with higher ammonia storage capacity; this effectively

compensates lower active-site concentrations. This is especially the case for nonsteady-state operations. For our Fe/SSZ-13 catalysts, ^{27}Al NMR results displayed in Figure 4a and NH_3 -TPD reported earlier¹⁹ demonstrate substantial loss of ammonia storage capacity upon hydrothermal aging. However, as shown in Figure 7a, SCR performance does not appear to correlate positively with ammonia storage capacity. At least under steady-state reaction conditions, Brønsted acidity appears to be less critical than the nature of Fe sites in standard SCR.

For the NH_3 oxidation reaction, we have shown recently that it is catalyzed by Fe-containing moieties larger than dimers, i.e., Fe-oxide clusters and particles.¹² As displayed in Figures 7c and S4c, fresh catalysts are more active than hydrothermally aged ones for this reaction. This seems to be discrepant with the fact that the contents of Fe-oxide clusters increase with hydrothermal aging. There are a few possible causes for the discrepancy. First, the same as standard SCR, this reaction is influenced by ammonia storage capacity of the catalyst. It appears that ammonia storage has stronger influence on ammonia oxidation than on standard SCR. Second, accessible surface site density for oxide clusters does not necessarily increase with increasing hydrothermal aging temperature because larger clusters expose lower percentages of surface sites. Lastly, Al incorporation into such clusters lowers their oxidation capacities as discussed above. In any case, it is important to note that hydrothermal aging does not diminish SCR selectivity for Fe/SSZ-13 catalysts because the side reaction, NH_3 oxidation, is not promoted. This is in stark contrast to Cu/SSZ-13 catalysts where hydrothermal aging does cause SCR selectivity drop.^{7,11}

5. CONCLUSIONS

During hydrothermal aging, Fe/SSZ-13 catalysts experience dealumination and Fe-ion agglomeration, the same as other Fe/zeolite SCR catalysts.^{17,55} However, because of the small pore size and remarkable structural stability of this material, unique properties not seen in other Fe/zeolite systems are found. These include (1) free Fe^{2+} ions that populate extensively in fresh samples convert to $[\text{HO-Fe-O-Fe-OH}]^{2+}$ dimers during hydrothermal aging; (2) $[\text{HO-Fe-O-Fe-OH}]^{2+}$ dimers maintain high stability; their contents do not decrease even in the HTA-800 sample; (3) Fe-oxide clusters with sizes measuring 1–2 nm form. These either populate inside individual SSZ-13 particles, presumably in secondary pores generated during aging, or on zeolite external surfaces. Detached Al interact strongly with Fe sites via the following mechanisms: some migrate out of SSZ-13 particles and incorporate into existing Fe-oxide particles prior to aging; some migrate into Fe-oxide clusters generated during aging; and the remaining interact individually with $[\text{HO-Fe-O-Fe-OH}]^{2+}$ dimers via acid–base interactions. These interactions render detached Al NMR invisible. In terms of catalytic properties, mild hydrothermal aging at 600 and 700 °C reduces inactive free Fe^{2+} thus enhancing SCR performance. Harsh aging at 800 °C causes strong Al inhibition to various Fe sites thus deteriorating SCR performance. NO and NH_3 oxidation activities can also be explained in terms of Fe-ion agglomeration and Al poisoning. For the latter, ammonia storage also plays a role.

■ ASSOCIATED CONTENT

Supporting Information

The Supporting Information is available free of charge on the ACS Publications website at DOI: 10.1021/acscatal.6b03679.

Surface area/pore volume analysis and XRD patterns of the samples; atom probe tomography sample preparation; APT analysis on Fe distribution in HTA-800 Fe/SSZ-13 sample; standard SCR, NO, and NH₃ oxidation reaction results, as well as NO formation during NH₃ oxidation on the 1.2% Fe-loaded fresh and HTA catalysts; and Arrhenius plots for standard SCR over (a) 0.37% and (b) 1.20% Fe-loaded fresh and hydrothermally aged Fe/SSZ-13 catalysts (PDF)

AUTHOR INFORMATION

Corresponding Author

*E-mail for F.G.: feng.gao@pnnl.gov.

ORCID

Nancy M. Washton: 0000-0002-9643-6794

Feng Gao: 0000-0002-8450-3419

Notes

The authors declare no competing financial interest.

ACKNOWLEDGMENTS

The authors gratefully acknowledge the U.S. Department of Energy (DOE), Energy Efficiency and Renewable Energy, Vehicle Technologies Office for the support of this work. The research described in this paper was performed in the Environmental Molecular Sciences Laboratory (EMSL), a national scientific user facility sponsored by the DOE's Office of Biological and Environmental Research and located at Pacific Northwest National Laboratory (PNNL). PNNL is operated for the U.S. DOE by Battelle.

REFERENCES

- (1) Beale, A. M.; Gao, F.; Lezcano-Gonzalez, I.; Peden, C. H. F.; Szanyi, J. *Chem. Soc. Rev.* **2015**, *44*, 7371–7405.
- (2) Kwak, J. H.; Tonkyn, R. G.; Kim, D. H.; Szanyi, J.; Peden, C. H. F. *J. Catal.* **2010**, *275*, 187–190.
- (3) Wijayanti, K.; Andonova, S.; Kumar, A.; Li, J. H.; Kamasamudram, K.; Currier, N. W.; Yezerets, A.; Olsson, L. *Appl. Catal., B* **2015**, *166–167*, 568–579.
- (4) Zhang, L.; Wang, D.; Liu, Y.; Kamasamudram, K.; Li, J. H.; Epling, W. *Appl. Catal., B* **2014**, *156–157*, 371–377.
- (5) Lezcano-Gonzalez, I.; Deka, U.; van der Bij, H. E.; Paalanen, P.; Arstad, B.; Weckhuysen, B. M.; Beale, A. M. *Appl. Catal., B* **2014**, *154–155*, 339–349.
- (6) Kim, Y. J.; Lee, J. K.; Min, K. M.; Hong, S. B.; Nam, I. S.; Cho, B. K. *J. Catal.* **2014**, *311*, 447–457.
- (7) Schmiege, S. J.; Oh, S. H.; Kim, C. H.; Brown, D. B.; Lee, J. H.; Peden, C. H. F.; Kim, D. H. *Catal. Today* **2012**, *184*, 252–261.
- (8) Kwak, J. H.; Tran, D.; Burton, S. D.; Szanyi, J.; Lee, J. H.; Peden, C. H. F. *J. Catal.* **2012**, *287*, 203–209.
- (9) Vennestrom, P. N. R.; Janssens, T. V. W.; Kustov, A.; Grill, M.; Puig-Molina, A.; Lundegaard, L. F.; Tiruvalam, R. R.; Concepcion, P.; Corma, A. *J. Catal.* **2014**, *309*, 477–490.
- (10) Luo, J. Y.; Wang, D.; Kumar, A.; Li, J. H.; Kamasamudram, K.; Currier, N. W.; Yezerets, A. *Catal. Today* **2016**, *267*, 3–9.
- (11) Gao, F.; Wang, Y. L.; Kollar, M.; Washton, N. M.; Szanyi, J.; Peden, C. H. F. *Catal. Today* **2015**, *258*, 347–358.
- (12) Gao, F.; Zheng, Y.; Kukkadapu, R. K.; Wang, Y. L.; Walter, E. D.; Schwenzer, B.; Szanyi, J.; Peden, C. H. F. *ACS Catal.* **2016**, *6*, 2939–2954.
- (13) Balle, P.; Geiger, B.; Kureti, S. *Appl. Catal., B* **2009**, *85*, 109–119.
- (14) Frey, A. M.; Mert, S.; Due-Hansen, J.; Fehrmann, R.; Christensen, C. H. *Catal. Lett.* **2009**, *130*, 1–8.
- (15) Klukowski, D.; Balle, P.; Geiger, B.; Wagloehner, S.; Kureti, S.; Kummerle, B.; Baiker, A.; Grunwaldt, J. D. *Appl. Catal., B* **2009**, *93*, 185–193.
- (16) He, C. H.; Wang, Y. H.; Cheng, Y. S.; Lambert, C. K.; Yang, R. T. *Appl. Catal., A* **2009**, *368*, 121–126.
- (17) Shwan, S.; Adams, E. C.; Jansson, J.; Skoglundh, M. *Catal. Lett.* **2013**, *143*, 43–48.
- (18) Gao, F.; Kollar, M.; Kukkadapu, R. K.; Washton, N. M.; Wang, Y. L.; Szanyi, J.; Peden, C. H. F. *Appl. Catal., B* **2015**, *164*, 407–419.
- (19) Gao, F.; Szanyi, J.; Wang, Y. L.; Schwenzer, B.; Kollar, M.; Peden, C. H. F. *Top. Catal.* **2016**, *59*, 882–886.
- (20) Gao, F.; Washton, N. M.; Wang, Y. L.; Kollar, M.; Szanyi, J.; Peden, C. H. F. *J. Catal.* **2015**, *331*, 25–38.
- (21) Gao, F.; Walter, E. D.; Washton, N. M.; Szanyi, J.; Peden, C. H. F. *ACS Catal.* **2013**, *3*, 2083–2093.
- (22) Szanyi, J.; Gao, F.; Kwak, J. H.; Kollar, M.; Wang, Y. L.; Peden, C. H. F. *Phys. Chem. Chem. Phys.* **2016**, *18*, 10473–10485.
- (23) Devaraj, A.; Colby, R.; Hess, W. P.; Perea, D. E.; Thevuthasan, S. *J. Phys. Chem. Lett.* **2013**, *4*, 993–998.
- (24) Devaraj, A.; Gu, M.; Colby, R.; Yan, P.; Wang, C. M.; Zheng, J. M.; Xiao, J.; Genc, A.; Zhang, J. G.; Belharouak, I.; Wang, D.; Amine, K.; Thevuthasan, S. *Nat. Commun.* **2015**, *6*, 8014.
- (25) Gao, F.; Walter, E. D.; Kollar, M.; Wang, Y. L.; Szanyi, J.; Peden, C. H. F. *J. Catal.* **2014**, *319*, 1–14.
- (26) Gao, F.; Walter, E. D.; Karp, E. M.; Luo, J. Y.; Tonkyn, R. G.; Kwak, J. H.; Szanyi, J.; Peden, C. H. F. *J. Catal.* **2013**, *300*, 20–29.
- (27) Chen, H. Y.; Sachtler, W. M. H. *Catal. Today* **1998**, *42*, 73–83.
- (28) Long, R. Q.; Yang, R. T. *J. Catal.* **1999**, *188*, 332–339.
- (29) Long, R. Q.; Yang, R. T. *J. Am. Chem. Soc.* **1999**, *121*, 5595–5596.
- (30) Klinowski, J. *Chem. Rev.* **1991**, *91*, 1459–1479.
- (31) Dubkov, K. A.; Ovanesyan, N. S.; Shteinman, A. A.; Starokon, E. V.; Panov, G. I. *J. Catal.* **2002**, *207*, 341–352.
- (32) Mul, G.; Perez-Ramirez, J.; Kapteijn, F.; Moulijn, J. A. *Catal. Lett.* **2002**, *80*, 129–138.
- (33) Gao, F.; Kwak, J. H.; Szanyi, J.; Peden, C. H. F. *Top. Catal.* **2013**, *56*, 1441–1459.
- (34) Fickel, D. W.; D'Addio, E.; Lauterbach, J. A.; Lobo, R. F. *Appl. Catal., B* **2011**, *102*, 441–448.
- (35) Jacob, K. T.; Alcock, C. B. *J. Am. Ceram. Soc.* **1975**, *58* (5–6), 192–195.
- (36) Meyers, C. E.; Mason, T. O.; Petuskey, W. T.; Halloran, J. W.; Bowen, H. K. *J. Am. Ceram. Soc.* **1980**, *63*, 659–663.
- (37) Gao, F.; Kollar, M.; Kukkadapu, R. K.; Washton, N. M.; Wang, Y. L.; Szanyi, J.; Peden, C. H. F. *Appl. Catal., B* **2015**, *164*, 407–419.
- (38) Kurtz, D. M. *Chem. Rev.* **1990**, *90*, 585–606.
- (39) Brandenberger, S.; Krocher, O.; Casapu, M.; Tissler, A.; Althoff, R. *Appl. Catal., B* **2011**, *101*, 649–659.
- (40) Proding, S.; Derewinski, M. A.; Wang, Y. L.; Washton, N. M.; Walter, E. D.; Szanyi, J.; Gao, F.; Wang, Y.; Peden, C. H. F. *Appl. Catal., B* **2017**, *201*, 461–469.
- (41) Senderov, E.; Halasz, I.; Olson, D. H. *Microporous Mesoporous Mater.* **2014**, *186*, 94–100.
- (42) Engelhardt, D.; Michel, D. *High Resolution Solid-State NMR of Silicates and Zeolites*; Wiley: New York, 1987.
- (43) Lynch, J.; Raatz, F.; Dufresne, P. *Zeolites* **1987**, *7*, 333–340.
- (44) Kawai, T.; Tsutsumi, K. *J. Colloid Interface Sci.* **1999**, *212*, 310–316.
- (45) Kumar, M. S.; Schwidder, M.; Grunert, W.; Bruckner, A. *J. Catal.* **2004**, *227*, 384–397.
- (46) Schwidder, M.; Kumar, M. S.; Klementiev, K.; Pohl, M. M.; Bruckner, A.; Grunert, W. *J. Catal.* **2005**, *231*, 314–330.
- (47) Santosh Kumar, M.; Schwidder, M.; Grunert, W.; Bentrup, U.; Bruckner, A. *J. Catal.* **2006**, *239*, 173–186.
- (48) Brandenberger, S.; Krocher, O.; Tissler, A.; Althoff, R. *Appl. Catal., B* **2010**, *95*, 348–357.
- (49) Velez, R. P.; Ellmers, I.; Huang, H. M.; Bentrup, U.; Schunemann, V.; Grunert, W.; Bruckner, A. *J. Catal.* **2014**, *316*, 103–111.

- (50) Li, J.; Li, S. H. *J. Phys. Chem. C* **2008**, *112*, 16938–16944.
- (51) Long, R. Q.; Yang, R. T. *J. Catal.* **2002**, *207*, 274–285.
- (52) Brandenberger, S.; Krocher, O.; Tissler, A.; Althoff, R. *Catal. Rev.: Sci. Eng.* **2008**, *50*, 492–531.
- (53) Ellmers, I.; Velez, R. P.; Bentrup, U.; Bruckner, A.; Grunert, W. *J. Catal.* **2014**, *311*, 199–211.
- (54) Ruggeri, M. P.; Selleri, T.; Colombo, M.; Nova, I.; Tronconi, E. *J. Catal.* **2014**, *311*, 266–270.
- (55) Brandenberger, S.; Krocher, O.; Casapu, M.; Tissler, A.; Althoff, R. *Appl. Catal., B* **2011**, *101*, 649–659.